Interfacial Roughening During Solid Phase Epitaxy: Interaction of Dopant, Stress, and Anisotropy Effects

William Barvosa-Carter and Michael J. Aziz***
Division of Engineering and Applied Sciences, Harvard University, Cambridge, MA
A.-V. Phan
Department of Mechanical Engineering, University of South Alabama, Mobile, AL

T.Kaplan, and L.J. Gray
Oak Ridge National Laboratory, Oak Ridge, TN

The effects of externally applied stress and rate-enhancing dopants on interfacial roughness during solid phase epitaxial growth of ion-implantation doped Si are investigated using cross-sectional transmission microscopy and time-resolved reflectivity. We find long-wavelength roughness in the absence of applied stress that arises solely from the dopant gradient. With the addition of compressive stress the interface roughens further with an enhanced magnitude and a dramatically reduced wavelength. We discuss the experimental results in the context of a simulation that includes our current understanding of stress, dopant-gradient, and interface anisotropy effects. We find a rich interplay between these effects in determining growth morphology evolution and demonstrate the successes and current limitations of the model.

(prepared for submission to the Journal of Applied Physics)

*Present address: HRL Laboratories, Malibu CA; wbc@hrl.com

**maziz@harvard.edu

I. Introduction

Band-gap engineering using strained-layer heteroepitaxy has become a useful tool for device designers looking to enhance and extend the capabilities of Si-based devices. As a result, an increasing number of Si-based devices involving strained layers are being investigated for use as high-speed field-effect transistors [1], heterojunction bipolar transistors [2], and photodetectors [3]. Many of these devices can be made readily with techniques such as Molecular Beam Epitaxy. The use of device heterostructures incorporating strained layers would become much more widespread if more cost-effective processes, such as ion-implantation followed by subsequent solid-phase epitaxial growth (SPEG) to restore crystallinity and activate dopants, could be used for their fabrication. Problems arise, however. For example, in the Si-Ge system, roughening of the amorphous-crystal (a-c) interface occurs above a Ge content of 3-7 at. %, followed by dislocation and stacking fault generation, leading to severely degraded material not suitable for devices. The observed interfacial roughening has been attributed [4,5] to the Asaro-Tiller-[6] / Grinfeld [7] (ATG) energetically-driven growth instability, wherein the elastic strain energy (due, in the case of SiGe SPEG, to the self-stress caused by Ge) is reduced by interface roughening.

The purpose of this work is to investigate the role of stress in interfacial roughening and defect generation during SPEG of Si, specifically in the presence of ion-implanted impurities that, like Ge [8], enhance the local interface velocity relative to that of pure Si. Compressive stress alone has been shown to destabilize the a-c interface during SPEG of Si and allow it to roughen [9,10]. The mechanism for this roughening does not arise from energetic concerns, as has been described by ATG, but instead from the effect of stress on the barriers to local kinetic growth processes [11,12]. In that earlier work, we determined that this new kinetically-driven instability, rather than the ATG instability, was primarily responsible for interfacial roughening during SPEG of Si.

In the absence of stress, the presence of a rate-enhancing impurity has also been shown to destabilize the interface [5]. This leads us to consider the case of SPEG of a strained layer that

contains a rate-enhancing impurity (such as a strained $Si_{1-x}Ge_x$ layer) as being more complicated because both composition and stress effects are present. Rather than attempt to decouple these effects in the complex Si-Ge system, we have chosen to study a simpler case where a dopant profile (B) is introduced that mimics the rate-enhancing effects of Ge [13] , but induces a negligible stress in the lattice. Instead of the inherent stress due to Ge composition, compressive stress is *mechanically* applied in the plane of the growth front. Similar stress states would be imposed by the substrate during SPEG of doped heteroepitaxial thin films. Additionally, B appears to be a good choice for mimicking the rate-enhancing effects of Ge: we have shown previously that effects of stress and dopant concentration are separable – leading to a simplified growth model [11]. Here we report a rich interplay between stress, dopant-gradient, and crystalline anisotropy effects in determining growth morphology evolution and demonstrate the successes and current limitations of a model incorporating our current understanding of these phenomena. It is anticipated that these same effects will be important in some scenarios involving deposition from a vapor, but despite the vast amount of literature devoted to processes such as MBE, to our knowledge there has been no exploration of these issues in that arena.

II. Experiment

The sample geometry and procedure used to measure in-plane stress effects on SPEG of Si has been described in detail elsewhere [10]. The samples for this study consisted of a-Si layers produced on 0.034" thick, double-side polished (001) silicon wafers by ion implantation ($^{28}Si^+$,1x10^{15}/cm^2 at 60 keV followed by 2x10^{15}/cm^2 at 180 keV and $^{11}B^+$, 5x10^{15}/cm^2 at 50 keV). This produced an approximately Gaussian depth distribution of B centered at ~150 nm deep in an ~320 nm thick a-Si film. The loading and optical geometry is shown schematically in Fig. 1. In this arrangement, a uniaxial stress σ_{11} was applied in the plane of the amorphous-crystal interface. In most of our experiments we applied stress along the [100] direction. A few samples were also annealed along [110], and no striking differences in behavior could be observed. Optical access enabled real-time measurement of the growth rate using time-resolved reflectivity (TRR) [13] monitored at λ=632.8 nm. All samples were pre-annealed for 1 hour at

450 °C, and then treated to varying magnitudes of stress, as described in the discussion section below.

Fig. 2 shows a series of cross-sectional TEM micrographs of several samples annealed for successively longer times. The initial interface (a) is shown after the pre-anneal at 450 °C for 1 hour: This initial interface is not completely flat, but has a roughness on the order of 2-3 nm. With subsequent annealing at 500 °C and a (compressive) stress of -0.5 GPa in the plane of the interface, however, the roughness of the sample evolves dramatically, increasing to a peak-to-trough roughness of ~25 nm at a depth of roughly 180 nm (b). The third micrograph (c) shows that the interface structure at 90 nm depth is roughly the same as at 180 nm. Relative to the zero-stress sample shown in Fig. 2(d), *the interface roughness is significantly enhanced when growth occurs under stress*. Additionally, a greatly enhanced density of dislocations can be seen penetrating from the interface down to the original position of the interface, marked by the end-of-range damage left from the implantation process. We suspect that these are most likely hairpin dislocations arising from the end-of-range damage and activated by the applied stress.

To investigate the time dependence of the evolution of the interface roughness, we annealed several stressed samples while monitoring TRR for as much of the regrowth as possible. Fig. 3 shows a comparison of TRR obtained from three samples annealed at stresses of 0 GPa, -0.25 GPa, and -0.5 GPa. Comparison of the raw data is difficult because the interface velocity changes with time due to the non-uniform boron doping. To facilitate comparison, this depth-dependent velocity has been deconvoluted from the experimental curve [14]. The –0.25 GPa sample could be completely crystallized under stress, but due to crack formation the –0.5 GPa sample could only be crystallized under stress to within 50 nm of the surface before the sample fractured. Comparing the three experimental curves to the calculated curve in Fig. 3, the most significant feature is that the amplitude of the TRR oscillations is reduced with increasing stress.

III. Analysis

Given the TEM results for the –0.5 GPa samples, it appears that the primary mechanism for the TRR amplitude reduction seen in Fig. 3 is roughening of the a-c interface. We extracted

interface roughness as a function of depth from the TRR data using the method of Zeng *et al*. [15] and the implementation given by Elliman and Wong [5] who took as their measure of interface roughness the full width of a normalized triangular distribution of interface depths. The method assumes that the spatial periodicity of the interface roughness is much greater than the wavelength of light in the amorphous phase (λ/n = 632.8 nm/4.85 = 130 nm). Making the opposite assumption does not change our conclusions. To extract quantitative values of the roughness from the TRR data, we match each maximum or minimum in the TRR curve to a reflectivity predicted theoretically assuming a symmetric triangular distribution of interface depths with full width at full maximum A. We find that such a triangular distribution is reasonable, with other functional forms fitting the depth distribution in our micrographs less well.

Fig. 4 gives values of A as a function of depth for each of the curves shown in Fig. 3. Generally, we find that A increases overall with increasing stress, and tends to follow the depth distribution of the dopant concentration. Significantly, it appears as though the 'zero stress' sample has non-zero roughness for most of the regrowth. At a microscopic level, we find that this is indeed the case, as shown in the micrograph in Fig. 5. While at short length scales (<100 nm, Fig. 2(d)) the interface is smooth, variations in interface position appear over much longer length scales ($\lambda \sim$ 800-1200 nm). The interface depth on average deviates about ±10 nm, which compares favorably with the value of A extracted from the TRR at the same depth.

The higher stress samples show increasing interface roughening (Fig. 4). The sample held at -0.25 GPa shows a trend similar to the roughness of the zero stress sample, in that the roughness increases until the peak of the B distribution is reached, and then, again following the decreasing B concentration, it decreases. The same trend is evident with the -0.5 GPa sample, except that after the interface passes through the peak of the boron distribution the roughness is sustained somewhat. This is consistent with the TEM results shown in Fig. 2(c). Additionally, we find that, while there is a clear enhancement of the interface roughness (~ ×1.5-2 at -0.5 GPa), stress induces a dramatic reduction in ω.

IV. Analytical modeling of roughness evolution

For the case of the zero stress samples, our understanding of the variations in interface depth is in terms of a dopant gradient-driven kinetic interface instability described by Elliman and Wong (EW) [5]. Their description of this process is analytical, and we present a comparison of our results to the predictions of their model. The EW interface roughening mechanism occurs when the interface is growing into a region of increasing rate-enhancing impurity content: initially depth-displaced segments of the interface move through the impurity distribution at different times, with their relative displacement essentially being magnified by the rate enhancement. EW show that as a result, the interface roughness A scales with the velocity distribution v(z) according to

$$A(z) = A(z_0)[v(z)/v(z_0)] , \quad (1)$$

where z is the average depth of the interface and $A(z_0)$ is the interface roughness at an abritrary reference depth z_0. We find that the zero-stress samples follow this relationship. In Fig. 4 we compare the zero-stress data to the EW model: the bold dashed curve is the velocity distribution extracted from the zero-stress TRR curve scaled by the interface roughness measured at a depth of ~150 nm from Fig. 5.

It is highly plausible that occurrence of roughness only for large lateral length scales (ω >800nm) for the stress-free case is attributable to crystalline anisotropy effects: v is drastically reduced as the local interface orientation tends away from (001) toward (111) [16]. The orientation effect prejudices the evolution toward a slope selection and dictates a maximum aspect ratio Γ for interface fluctuations; hence *for a given A there is a minimum value of* ω. An additional consequence of the anisotropy effect is that an initially rough interface in the absence of stress or dopants tends to be smoothed out as faster (001) trailing segments overtake slower, sloped segments. As a result, in the absence of stress the EW mechanism amplifies only large ω.

The EW model does not permit the prediction of stress effects on interface roughness. To more fully understand the interacting factors of stress, dopant gradients, and kinetic anisotropy, we turn to a detailed model developed previously [9,17]. This model incorporates sufficient

detail to capture several possible mechanisms for stress effects on interfacial roughening, including the ATG instability [6,7] and the stress-induced kinetically-driven instability we have described previously [9]. Both the ATG and stress-induced kinetically-driven instabilities are predicted to enhance the interface roughness under compressive stress, becoming more effective at larger Γ. In addition to these stress-induced instabilities, the EW mechanism will also act to amplify the interface roughness. Currently within the model, kinetic anisotropy is the only effect providing any kind of "damping." (Capillary forces due to the interface energy are several orders of magnitude too small to have any effect on interface evolution within the current model.) A simple analytical treatment of the interface morphology due to these effects is difficult to obtain for large Γ: while deviations from (001) and B concentration are local effects, the stress on each local segment of the interface depends on the overall morphology. For a description of the complex interplay between these processes as the interface evolves into the large Γ regime, we turn to numerical simulation techniques.

V. Numerical simulations of interface evolution

The simulations are based on a coupling of the boundary contour method (BCM) and level set methods. The BCM (e.g., [18]) is used to evaluate displacements and boundary stresses on the crystal interface, and tractions on the amorphous interface. Level set methods track the evolution of this crystalline/amorphous interface. This work uses a NarrowBand level set formulation [19] to characterize and advance the evolving interface. For details about the theory, algorithms, and applications of level set methods, the reader is referred to [20].

We consider a two-phase amorphous-Si/crystal-Si system subjected to non-hydrostatic compressive σ_{11}. Three cases of stress, namely σ_{11} = -0:5; -0:25 and 0 GPa are studied. The interface of the system is initially modeled as a sine wave as described in figure 6, with an imposed wavelength and initial amplitude A_0 to be determined by comparison between the final morphologies of experiments and simulations. Because we have so little information about the roughness spectrum before growth, the starting wavelength in the simulations was fixed at 900 nm, a value chosen somewhat arbitrarily because the results are fairly insensitive to wavelength

in this regime. By symmetry, only a half wavelength segment needs to be treated. The silicon crystal is modeled as an isotropic linear elastic solid with a shear modulus $G_c = 0.6814 \times 10^{11}$ Pa and Poisson ratio $\nu_c = 0.2174$ [21]. The amorphous solid is modeled by Stokes flow with a time dependent viscosity to reflect structural relaxation [17] We assume plane stress for the elastic solids analyses.

The interface velocity v (normal to the interface) is determined by using Eq. (1) in reference [17],

$$\mathrm{v}\left(\theta, C, \boldsymbol{\sigma}, \kappa; T\right) = \mathrm{v}_0\left(\theta\right) f\left(C\right) \exp\left(\frac{\boldsymbol{\sigma} : \mathbf{V}^* - E^*}{k_B T}\right) \sinh\left(\frac{\Delta G_{ac}\left(\boldsymbol{\sigma}, \kappa; T\right)}{2 k_B T}\right) \qquad (2)$$

where θ is interface misorientation relative to (001), C is the concentration of dopant, $\boldsymbol{\sigma}$ is the local stress tensor at the interface, κ is the local curvature of the interface, v_0 is the velocity of an undoped stress-free planar interface, f(C) is discussed below, $\mathbf{V}^*$ is the activation strain tensor, E* is the activation energy, k_B is Boltzmann's constant, and ΔG_{ac} is the driving free energy, which includes contributions from capillarity, elastic strain energy density in both phases, and stress-strain work done on the surroundings.

We refer the reader to reference [17] for the details. Significantly, we include in the function for v parameters that, with appropriate values, allow expression of both the ATG instability (through changes in ΔG_{ac}) as well as the stress-induced kinetically-driven instability. In order to take into account the rate-enhancing effects of the B distribution in f(C), we *directly* use the measured velocity as the base velocity function as we did in the previous section. While some errors in the measurement of the velocity itself as well as errors due to the non-planarity of the interface are introduced by this method, we avoid complications arising from needing to accurately model the rate-enhancing effects of the B distribution.

The framework employed to determine the interface growth [17] can be described as follows. At each time step of the growth simulation the traction (normal component of the stress tensor) on the crystal interface is initially assigned its converged value from the previous time step. Next the crystal elasticity problem is solved using the BCM for elasticity with the new interface

position. In order to obtain a solution obeying traction continuity across the interface, the flow velocity boundary condition for the viscous amorphous material at the interface must be determined. This velocity, $\mathbf{v_a}$, is evaluated as the change in elastic displacement $\Delta\mathbf{u}$ of the crystal at each point along the interface caused by the strain energy relaxation solved for by the BCM [22], distributed over the growth time step Δt, by $\mathbf{v_a} = \Delta\mathbf{u}/\Delta t$. Once $\mathbf{v_a}$ is determined, the traction $\boldsymbol{\tau}_\mathbf{a}$ on the amorphous interface is found by solving the amorphous viscous flow problem using the BCM for Stokes flow. The traction on the amorphous interface at the i^{th} iteration, $\boldsymbol{\tau}_\mathbf{a}^{(i)}$, is used to update the traction $\boldsymbol{\tau}_\mathbf{c}^{(i+1)}$ of the subsequent iteration on the crystal interface using $\boldsymbol{\tau}_\mathbf{c}^{(i+1)} = \boldsymbol{\tau}_\mathbf{c}^{(i)} + k_r \boldsymbol{\tau}_\mathbf{a}^{(i)}$ where k_r is a relaxation coefficient, and the calculation is iterated to convergence.

Upon convergence, the other components of the boundary stress tensor on the crystal interface are computed using a post processing BCM routine. The interface velocity v is then determined by substituting the boundary stress into Eq. (2). Finally, v is supplied to a level set package in order to advance the crystal interface for the given time step Δt. [23]

VI. Simulation results and discussion

Our simulation results of the roughness (peak to peak amplitude A) versus depth for applied stresses of 0 GPa, -0.25 GPa, and -0.5 GPa, for both the simulation and experiment have been presented in Fig. 4. As stated in the previous section, the only adjustable parameter in these calculations is the peak-to-peak amplitude A_0 of the initial interface corrugation, chosen to best match the evolution of the roughness as measured in the experiment. The velocity distribution as a function of depth, the stress state and the effects of stress are all factors fixed by experiment. The simulation results are generally in agreement with the experimental trend of increasing stress causing increased interface roughening.

Although we find reasonable agreement between simulation and experiment if the initial wavelength in simulation is held fixed at 900 nm, the model does not permit us to understand how the selected wavelength varies with stress. If we consider a family of simulations in which the initially imposed wavelength is permitted to vary and the initial amplitude is held constant, the simulations appear to disagree *qualitatively* with the observations: in experiment, we

observe a characteristic wavelength dominating the final morphology that decreases with increasing applied compressive stress (e.g. compare Fig. 2 and Fig. 5), whereas the simulations, assuming a wavelength-independent initial amplitude, predict no such characteristic wavelength. Rather, the simulations predict a maximum roughness (i.e., at the peak of the boron profile) that is independent of wavelength for long wavelengths, with a cutoff for wavelengths below ~500 nm, as shown in Fig. 7.

In the linear regime of the model we would expect the wavelength that exhibits the maximum amplification rate to be chosen by competition between the various roughening and smoothening effects, which have different dependences on wavelength. We expect dopant-gradient-induced kinetic roughening to be independent of wavelength. We expect compressive stress to most rapidly amplify short wavelengths, where stress concentrations are greatest, and not amplify sufficiently long wavelengths, where stress concentrations are negligible [24]. We expect kinetic anisotropy to return the interface to planarity because off-[001] orientations have lower mobilities so the trailing [001] segments "catch up" and readily overtake the off-oriented segments; for a given amplitude this effect should be strongest at short λ, where the broadest range of orientations is exposed, and vanish at long λ. The effect of capillarity, another restoring force common to most morphological stability problems, is negligible in our case because the chemical contribution to the driving free energy ΔG_{ac} in Eq. (2) is always very large in magnitude compared to the capillary contribution. It may be that in the absence of an effect that preferably damps long-wavelength perturbations, the final roughness spectrum is very sensitive to the long-wavelength components of the initial roughness spectrum.

The cutoff at short λ in the simulations in Fig. 7 takes the form of a maximum observed aspect ratio Γ. This observation indicates that in the case of strongly driven roughening, kinetic anisotropy may serve only to limit amplification beyond a maximum aspect ratio, rather than provide any significant restoring force for smaller aspect ratios. If, at small amplitudes, the amplifying effect of stress overwhelms the restoring force of anisotropy for small wavelengths, a kinetically selected slope and aspect ratio may result from the nonlinear turn-on of anisotropy-

induced damping at large amplitude. Hence, in the low-λ regime, there may no mechanism for wavelength selection. Also, within the model, there could also be a strong, possibly nonlinear, interplay between stress-induced and dopant-gradient-induced kinetic roughening (which mutually reinforce one another through the interface morphology), and kinetic anisotropy. It is possible that the nonlinearities in Eq. (2) imply that any simulation of the evolution of a single Fourier component is not going to reproduce important experimental trends, in which case further progress may require simulation of starting profiles with experimentally determined initial roughness spectra.

Although there are factors that are not included in the simulation, such as an unknown initial roughness spectrum, a third dimension, and unknown dopant effects on off-(001) orientations, this disagreement with experiment on observed wavelength may indicate that a significant mechanism is absent in the simulations. Fig. 2. indicates that a somewhat narrow range of λ is preferentially amplified by stress. Several alternative mechanisms may explain this effect. The foremost feature aside from the increased interface roughness that appeared upon application of stress was a network of hairpin dislocations. The spatial distribution of these dislocations, and the concomitant local non-uniformities in stress along the interface, may be responsible for choosing a wavelength. If this is indeed the case, the model for solid phase epitaxy would have to be extended to include the kinetics of dislocation generation, perhaps in a similar vein to those for lattice-mismatched films grown from the vapor [25] or thermal stresses in growth from the melt [26]. Another possibility is that the ATG instability is more effective than our model would predict. In fact, the ATG instability has qualitative behavior that matches our observations: smaller λ should arise at increasing magnitude of stress. However, within currently accepted models for crystal growth some factor, such as the bulk driving free energy, the interfacial energy or the volume change upon crystallization, would need to be one or two orders of magnitude different than has been assumed, which seems unlikely.

VII. Summary

We find that stress and dopant gradient effects are both important in determining interface roughness evolution during SPEG of doped a-Si layers. In the absence of stress, roughening occurs due to dopant gradient effects. The Elliman-Wong model describes the roughness amplitude evolution quantitatively. We attribute the development of a large lateral length scale to selective damping of short wavelengths by kinetic anisotropy.

The application of compressive in-plane stress causes significantly increased roughening and a dramatic decrease in lateral length scale. When the sign of either the dopant concentration gradient [11] or the stress [27] is reversed, these factors become stabilizing, rather than destabilizing. In either case alone, past work shows excellent agreement between our model and experimental observations of SPEG of doped Si. When *both* these effects are included and are *destabilizing*, we find that the model accounts for roughness evolution vs. depth and applied stress if the wavelength is held fixed; however, its wavelength selection vs. stress is qualitatively opposite to experiment. We hypothesize that this is either because the nonlinearities inherent in the model render invalid the modeling approach that starts with a single Fourier component, or that some active mechanism is not present in our model.

Acknowledgements

We gratefully acknowledge stimulating discussions with G. Olson, J.A. Roth, and J. Kysar. Research at Harvard was supported by NSF grant DMR-0213373. Research at ORNL was supported in part by the Applied Mathematical Sciences Research Program of the Office of Mathematical, Information, and Computational Sciences, US Department of Energy under Contract Number DE-AC05-00OR22725 with UT-Battelle. A.-V. Phan acknowledges the support from University of South Alabama Research Council.

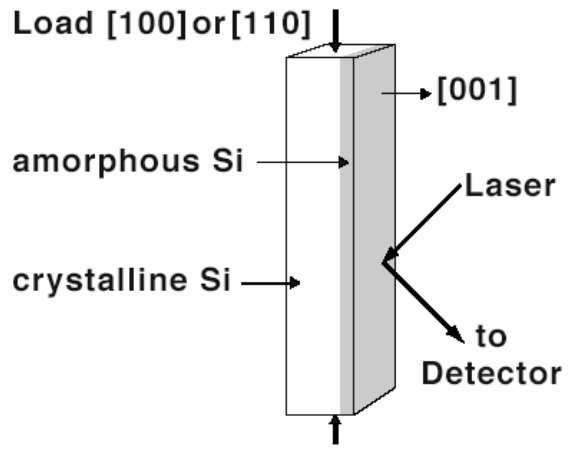

Fig. 1. Experimental geometry.

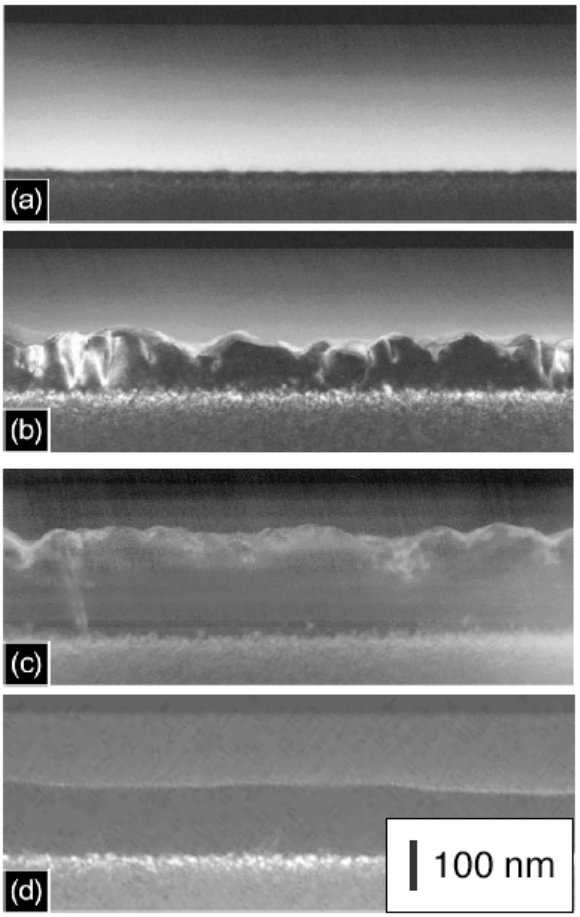

Fig. 2. Evolution of the amorphous-crystal interface: (a) initial interface; (b) after 90 nm growth and a compressive uniaxial stress of -0.5 GPa applied parallel to the interface in the plane of the page; (c) after 180 nm growth and a compressive stress of -0.5 GPa and (d) after 150 nm growth in the absence of stress.

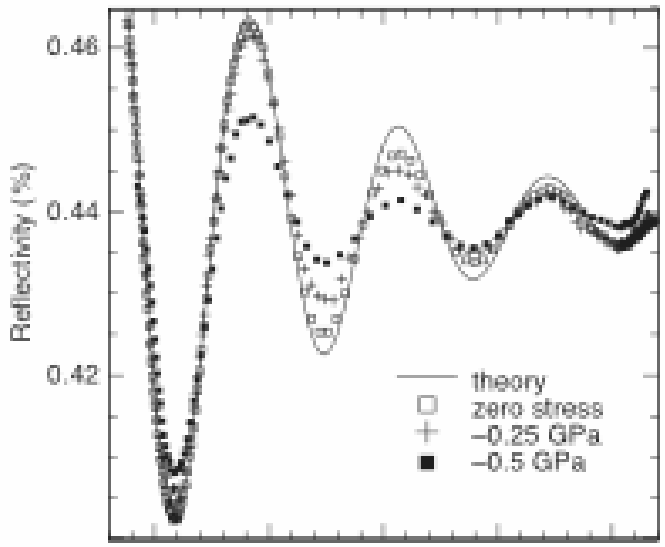

Fig. 3. Sample reflectivity vs. average interface depth for $\sigma_{11} = 0$ GPa, –0.25 GPa, and –0.5 GPa.

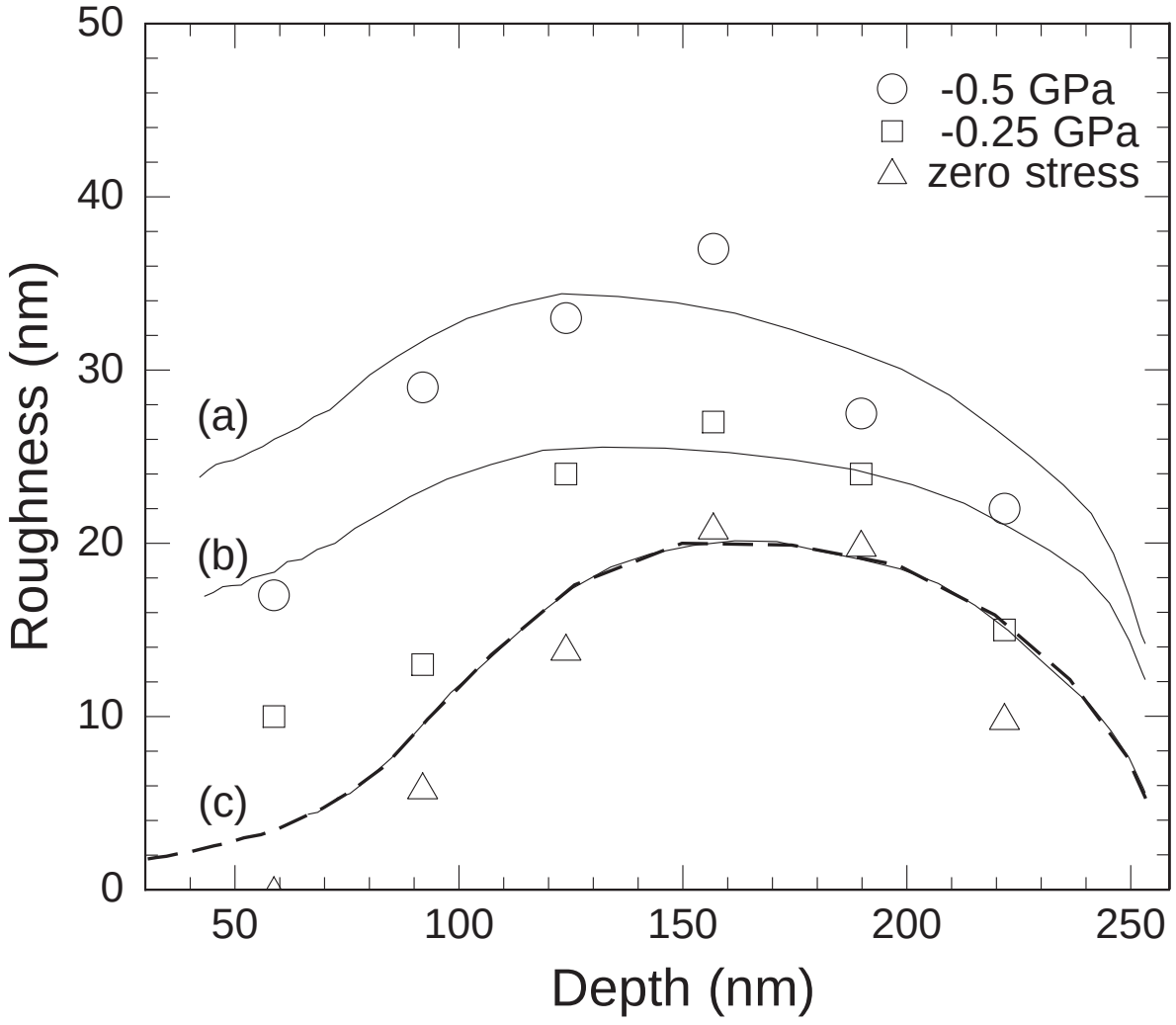

Fig. 4. Interface roughness vs. depth. Data points are extracted from the reflectivity in Figure 3. Bold dashed line: Elliman-Wong model for zero stress. Thin solid lines: our simulated roughness evolution as described in the text using, from top to bottom, (a) σ_{11} = -0.5 GPa, A_0 = 6.5 nm; (b) σ_{11} = -0.25 GPa, A_0 = 5.5 nm; (c) σ_{11} = 0 GPa, A_0 = 0.72 nm.

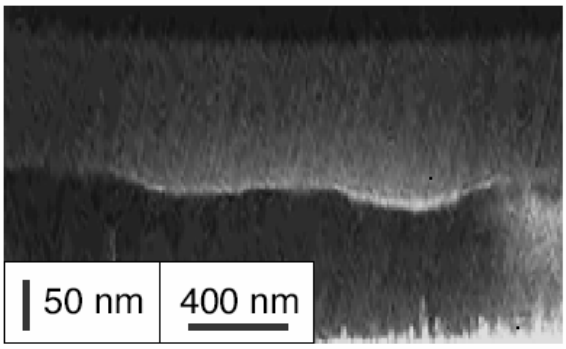

Fig. 5. Interface morphology at 150nm depth after annealing with zero stress. To enhance the visibility of the interface corrugation, the lateral scale has been compressed by a factor of 4 relative to the vertical scale.

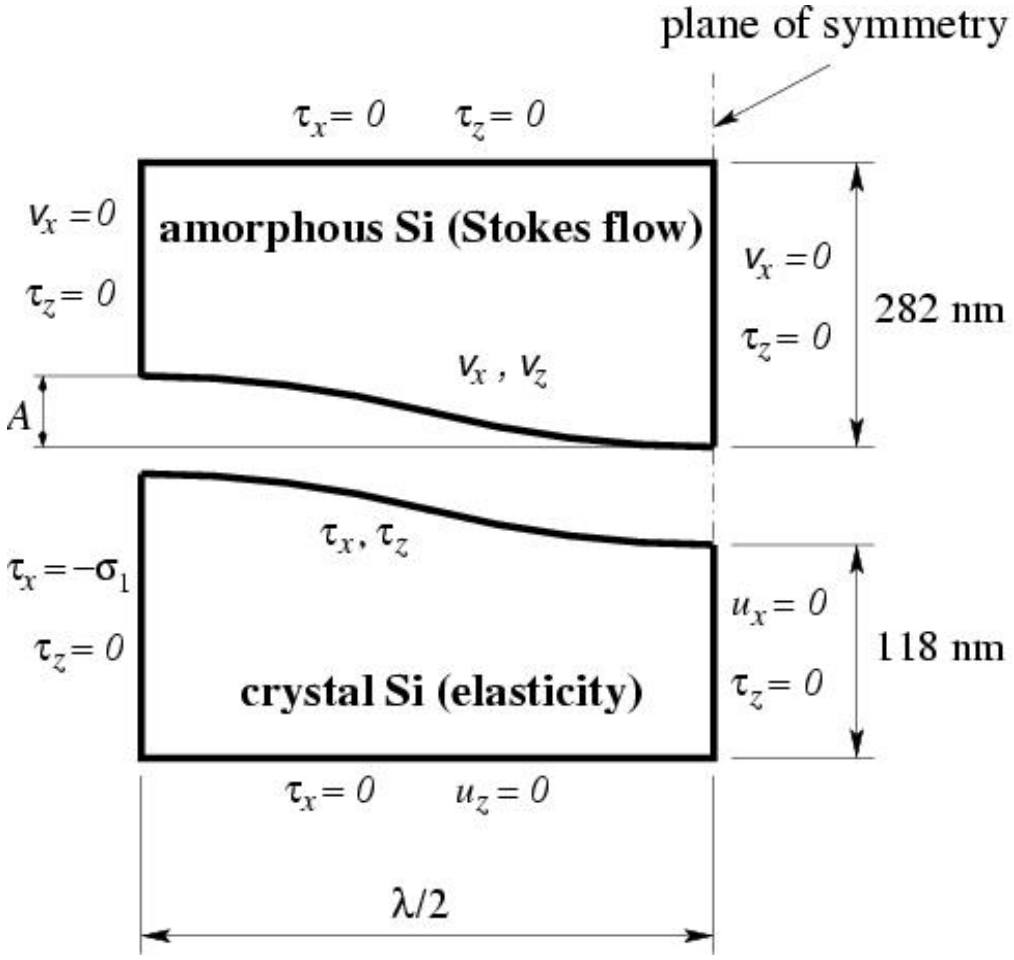

Fig. 6: Breakdown of geometry and boundary conditions for the simulation

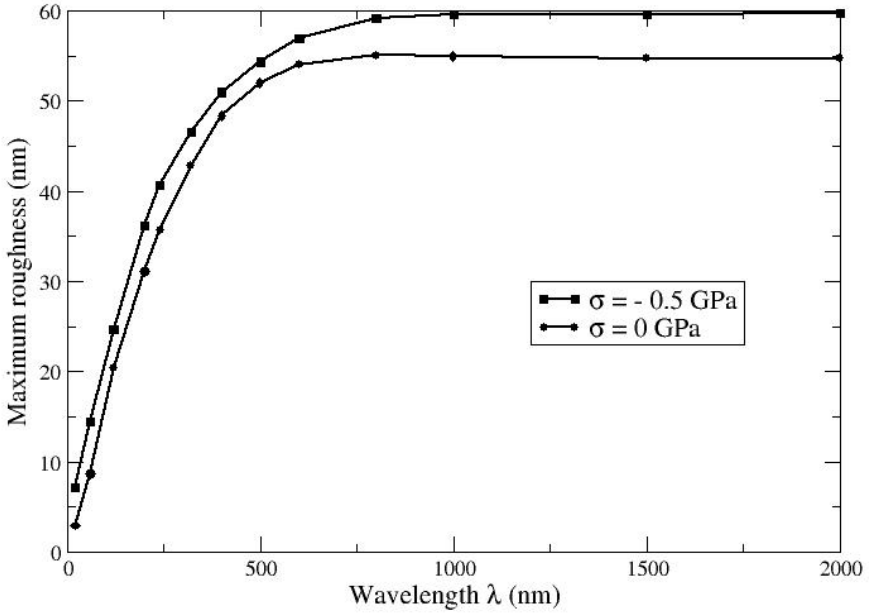

Fig. 7: Maximum roughness over the course of a simulation vs. wavelength λ for an initial amplitude $A_0 = 2$ nm and applied stress of -0.5 GPa and 0 GPa.

References

[1]W. Lu, S.J. Koester, X.-W. Wang, J.O. Chu, T.-P. Ma, and I. Adesida, *Journal of Vacuum Science and Technology B* **18**, 3488 (2000).
[2]L.E. Larson, *Journal of Vacuum Science and Technology B* **16**, 1541 (1998).
[3]H. Presting, J. Konle, M. Hepp, H. Kibbel, K. Thonke, R. Sauer, E. Corbin, and M. Jaros, *Optical Engineering* **39**, 2624 (2000).
[4]F. Corni, S. Frabboni, R. Tonini, and G. Ottaviani, *J. Appl. Phys.* **79**, 3528 (1996).
[5]R.G. Elliman and W.C. Wong, *Appl. Phys. Lett.* **69**, 2677 (1996).
[6]R.J. Asaro and W.A. Tiller, *Metall. Trans.* **3**, 1789 (1972).
[7]M.A. Grinfeld, *Sov. Phys. Dokl.* **31**, 831 (1986).
[8]T.E. Haynes, M.J. Antonell, C.A. Lee, and K.S. Jones, *Physical Review B* **51**, 7762 (1995).
[9]W. Barvosa-Carter, M.J. Aziz, L.J. Gray, and T. Kaplan, *Phys. Rev. Lett.* **81**, 1445 (1998).
[10]W. Barvosa-Carter and M.J. Aziz, *Mater. Res. Soc. Symp. Proc.* **441**, 75 (1997).
[11]W. Barvosa-Carter and M.J. Aziz, *Appl. Phys. Lett.* **79**, 356 (2001).
[12]M.J. Aziz, P.C. Sabin, and G.Q. Lu, *Physical Review B* **44**, 9812 (1991).
[13]G.L. Olson and J.A. Roth, "Solid Phase Epitaxy," in *Handbook of Crystal Growth, Volume 3, Chapter 7*, edited by D.T.J. Hurle (Elsevier, North Holland, 1994).
[14]J.C. McCallum, *Appl. Phys. Lett.* **69**, 925 (1996).
[15]X. Zeng, T.-C. Lee, J. Silcox, and M.O. Thompson, *Mater. Res. Soc. Symp. Proc.* **321**, 503 (1994).
[16]L. Csepregi, E.F. Kennedy, J.W. Mayer, and T.W. Sigmon, *J. Appl. Phys.* **49**, 3906 (1978).
[17]A.-V. Phan, T. Kaplan, L.J. Gray, D. Adalsteinsson, J.A. Sethian, W. Barvosa-Carter, and M.J. Aziz, *Modelling and Simulation in Materials Science and Engineering* **9**, 309 (2001).
[18]A.V. Phan, S. Mukherjee, and J.R.R. Mayer, *Computational Mechanics* **20**, 310 (1997); A.-V. Phan, L.J. Gray, T. Kaplan, and T.-N. Phan, *Computational Mechanics* **28**, 425 (2002).
[19]D. Adalsteinsson and J.A. Sethian, *J. Comput. Phys.* **118**, 269 (1995).
[20]J.A. Sethian, *Level Set Methods and Fast Marching Methods* (Cambridge University Press, 1999).
[21]A. Witvrouw and F. Spaepen, *J. Appl. Phys.* **74**, 7154 (1993).
[22]The velocity due to the rate of phase transformation from amorphous to crystal, Eq. (2), does not directly affect the viscous material because material is changing identity from amorphous to crystal, but not moving. The effects of the exceedingly small volume change during the phase transformation are already included in the measured values used for v0. The rate of phase transformation affects the flow velocity boundary condition only indirectly through the shape change that occurs during crystal growth.
[23]Note that the mesh of the new interface provided by level set methods could be highly non-uniform. This non-uniformity arises as a result of the fixed grid Eulerian setting employed by level set methods, where two nodes on a new front can be very close to each other. However, this non-uniform mesh can directly be employed by the BCM without degenerating the result accuracy as all boundary integrals are evaluated analytically in the BCM for 2-D calculations.
[24]P.W. Voorhees and M.J. Aziz, "The Effects of a Stress-Dependent Mobility on Interfacial Stability," in *Interfaces for the Twenty-First Century: New Research Directions in Fluid*

Mechanics and Materials Science, edited by M.K. Smith, M.J. Miksis, G.B. McFadden, G.P. Neitzel and D.R. Canright (Imperial College Press, London, 2002), pp. 167.
[25]C.W. Leitz, M.T. Currie, A.Y. Kim, J. Lai, E. Robbins, E.A. Fitzgerald, and M.T. Bulsara, *J. Appl. Phys*. **90**, 2730 (2001).
[26]X.A. Zhu and C.T. Tsai, *J. Appl. Phys.* **88**, 2295 (2000).
[27]J.F. Sage, W. Barvosa-Carter, and M.J. Aziz, *Appl. Phys. Lett.* **77**, 516 (2000).